Iraqi National Journal of Earth Science
www.earth.mosuljournals.com

Using Insar Time Series to Estimate Ground Displacement Resulting From 7.3 Mw 12 November 2017, Earthquake, Near the Iraq-Iran Border

Mohammad W. Al-zaidy [1*], **Ali K. Al-Ali** [2]

[1,2]*Department of Geology, College of Science, University of Basrah, Basrah, Iraq.*

Article information

Received: 25- Apr -2023

Revised: 02- May -2023

Accepted: 17- Jul -2023

Available online: 01- Jan – 2024

Keywords:
Earthquakes source-observations
Copernicus Sentinel-1
Zagros Front Fault
two-dimensional -Displacement
InSAR

Correspondence:
Name: Mohammad W. Al-zaidy

Email:
scipg.mohammad.waled@uobasrah.edu.iq

ABSTRACT

To comprehensively comprehend the potential risks posed by seismic activity and the formation of geological structures in areas with high tectonic activity, it is critical to conduct thorough investigations on the deformation of the Earth's crust caused by earthquakes. By analyzing the changes in the crust's shape and movements resulting from seismic events, researchers can gain valuable information on the underlying geological processes and the potential for future earthquakes. This knowledge can help in developing effective strategies to mitigate the impact of earthquakes on society and infrastructure, as well as contribute to a deeper understanding of the Earth's dynamic systems. In this study, we use Sentinel-1 interferometric synthetic aperture radar (InSAR) images, extending across a combination of two tracks that ascend and two tracks that descend. Two well-known processing methods, LiCSAR and LiCSBAS, were utilized to create the seismic deformation field and produce a time series of 2D deformation. One of the most powerful earthquakes to strike the region since 1900 happened on November 12, 2017, in Sarpol Zahab City located at the Iraq-Iran border. Another series of seismic events occurred approximately 100 kilometers to the south, near Mandali-Sumar in Iraq, on January 11, 2018. These earthquakes were noteworthy due to their intensity and proximity to populated areas, highlighting the potential risks and dangers associated with seismic activity in the region. This paper aims to create a map of neotectonics deformation of the ground along the Iraq-Iran borders from 2014 to 2022 and detect fault activity because of the earthquakes that occurred on November 12 and January 11, 2018, using inSAR techniques and confirmation on the processing, dissection, and applications of Sentinel-1 data backed by field, and tectonic information. The time series of 2D seismic deformation demonstrated a gradual decreasing pattern, which corresponded well with the distribution of aftershocks. The results show that the deformation for the Sarpol Zahab region extends to an area of 70 km2 and 90 km2, the greatest line-of-sight displacement of horizontal deformation is 20 cm and vertical displacement is 100 cm uplifting and 35 cm subsidence. The results of deformation for the Mandali-Sumar region extend to an area of 27 km2 and 23 km2, the greatest line of sight displacement of horizontal deformation is 5 cm and vertical displacement is 20 cm uplifting and 5 cm subsidence for ascending and descending data, respectively. The outcomes of this research will provide valuable insights into the investigation of tectonic events occurring in the region.

DOI: 10.33899/earth.2023.139927.1077, ©Authors, 2024, College of Science, University of Mosul.
This is an open-access article under the CC BY 4.0 license (http://creativecommons.org/licenses/by/4.0/).

استخدام السلاسل الزمنية لـ InSAR لتقدير النزوح الأرضي الناتج عن زلزال Mw 7.3 في 12 نوفمبر 2017، بالقرب من الحدود العراقية الإيرانية

محمد وليد الزيدي[1*], علي خالد العلي[2]

[2،1] قسم علم الأرض، كلية العلوم، جامعة البصرة ، البصرة ، العراق.

معلومات الارشفة

تاريخ الاستلام: 25- ابريل -2023

تاريخ المراجعة: 02- مايو -2023

تاريخ القبول: 17- يوليو -2023

تاريخ النشر الالكتروني: 01- يناير -2024

الكلمات المفتاحية:

رصد مصادر الزلازل

كوبرنيكوس الحارس -1

صدع زاغروس الأمامي

النزوح ثنائي الأبعاد inSAR

المراسلة:

الاسم: محمد وليد الزيدي

Email: scipg.mohammad.waled@uobasrah.edu.iq

الملخص

لفهم شامل للمخاطر المحتملة التي يشكلها النشاط الزلزالي وتشكيل الهياكل الجيولوجية في المناطق ذات النشاط التكتوني العالي، من المهم إجراء تحقيقات شاملة حول تشوه قشرة الأرض الناجمة عن الزلازل. من خلال تحليل التغيرات في شكل القشرة وحركاتها الناتجة عن الأحداث الزلزالية، يمكن للباحثين الحصول على معلومات قيمة عن العمليات الجيولوجية الأساسية وإمكانية حدوث الزلازل المستقبلية. يمكن أن تساعد هذه المعرفة في وضع استراتيجيات فعالة للتخفيف من تأثير الزلازل على المجتمع والبنية التحتية، فضلاً عن المساهمة في فهم أعمق للأنظمة الديناميكية للأرض. في هذه الدراسة، نستخدم صور رادار الفتحة الاصطناعية التداخل (InSAR) Sentinel-1، التي تمتد على مسارين تصاعديين ومسارين تنازليين. لبناء مجال التشوه الزلزالي والحصول على سلسلة زمنية من التشوه ثنائي الأبعاد، استخدمنا نظامين للمعالجة هما LiCSAR وLiCSBAS. وقع أحد أقوى الزلازل التي ضربت المنطقة منذ عام 1900 في 12 نوفمبر 2017، في مدينة سربول زاهاب الواقعة على الحدود العراقية الإيرانية. وقعت سلسلة أخرى من الأحداث الزلزالية على بعد حوالي 100 كيلومتر إلى الجنوب، بالقرب من مندلي سومر في العراق، في 11 يناير 2018. كانت هذه الزلازل جديرة بالملاحظة بسبب شدتها وقربها من المناطق المأهولة بالسكان، مما يسلط الضوء على المخاطر والأخطار المحتملة المرتبطة بالنشاط الزلزالي في المنطقة. الهدف من هذه الورقة هو إنشاء خريطة للتشوه التكتوني الحديث للأرض على طول الحدود العراقية الإيرانية من عام 2014 إلى عام 2022 والكشف عن نشاط الفوالق نتيجة للزلازل التي وقعت في 12 نوفمبر و11 يناير 2018، باستخدام تقنيات inSAR والتأكيد على معالجة وتحليل وتطبيق بيانات Sentinel-1 المدعومة بالميدان والمعلومات التكتونية. أظهرت السلسلة الزمنية للتشوه الزلزالي ثنائي الأبعاد نمطا متناقصا بصورة تدريجية، والذي يتوافق بشكل جيد مع توزيع الهزات الارتدادية. تظهر النتائج أن تشوه منطقة ساربول زاهاب يمتد إلى مساحة 70 كم2 و90 كم2، والحد الأقصى لخط إزاحة البصر للتشوه الأفقي هو 20 سم والإزاحة الرأسية 100 سم صعود وهبوط 35 سم. تمتد نتائج التشوه لمنطقة ماندلي سومار إلى مساحة 27 كم2 و23 كم2، والحد الأقصى لخط إزاحة البصر للتشوه الأفقي هو 5 سم والإزاحة الرأسية هي رفع 20 سم وهبوط 5 سم للبيانات الصاعدة والتنازلية، على التوالي. ستوفر نتائج هذا البحث رؤى قيمة حول التحقيق في الأحداث التكتونية التي تحدث في المنطقة.

DOI: 10.33899/earth.2023.139927.1077, ©Authors, 2024, College of Science, University of Mosul.
This is an open-access article under the CC BY 4.0 license (http://creativecommons.org/licenses/by/4.0/).

Introduction

Assessing earthquake damage requires an understanding of subsurface fault structures, as the location and shape of the fault have a significant impact on the level of damage near the epicenter (Jackson and Fitch, 1981). However, the expectation of the geometry and location of future fault ruptures is typically challenging. To estimate the seismic risk for each region about

impending earthquakes, it is crucial to determine the position and geometry of past earthquakes as well as identify faults in the area. This approach is useful in predicting the potential impact of future earthquakes and informing the development of effective mitigation strategies. Research studies have emphasized the importance of estimating fault parameters in earthquake-prone regions to improve our understanding of earthquake risk and prevent or minimize future damage (Motagh et al., 2014).

The collision between the Arabian and Eurasian plates during the (Middle Miocene) period generated the Zagros orogenic belt, which is known for being one of the youngest and most active intra-continental belts worldwide (Sharland et al., 2004). The Zagros Mountain range, oriented in an N 130° E direction, exhibits varying widths along its length. The range is approximately 200 km wide in the northern and southern regions, while it narrows down to less than 100 km in the central area (Abdulnaby et al., 2020; Vajedian et al., 2018b).

The recent earthquake that occurred in Iran was situated in the northwest of the Zagros Fold-Thrust Belt region, which is composed of various fault structures, as shown in Fig.1, these faults are mainly characterized by an overthrust structure, and the area is delineated by four main faults: the Main Recent Fault (MRF), the High Zagros Fault (HZF), the Mountain Front Fault (MFF), and the Zagros Foredeep Fault (ZFF) (VergÉS et al., 2011; Vernant et al., 2004). As such, it is imperative to conduct an extensive investigation into the co- and post-seismic deformation of the earthquake to understand the kinematics and geometry of the structures in this region. Such a study will enable scientists to expect future seismic activities and their trends, providing crucial insights into the geology and tectonic processes of the Zagros Fold-Thrust Belt (Vajedian et al., 2018b).

The European Space Agency launched the Sentinel-1 constellation, which includes two satellites, in 2014 and 2016. This satellite system can deliver high-quality Synthetic Aperture Radar (SAR) observations in the c-band. The SAR imagery has a moderate spatial resolution, ranging from 2 to 14 meters, and is obtained at a temporal resolution of 6 to 12 days. The sentinel-1 constellation captures both ascending and descending data and is particularly useful for monitoring tectonic deformation in various regions (Potin et al., 2018).

InSAR detectability and excellent spatial resolution in the epicentral region of shallow inland earthquakes have emerged as one of the technology's primary benefits in recent years, which can frequently provide the actual location of shallow moderate magnitude earthquakes (Gan et al., 2018; Qu et al., 2019). As of now, InSAR is often used to get highly accurate measurements of ground surface deformation (Sousa et al., 2014; Zhou et al., 2019). By utilizing a stack of SAR images, InSAR time series analysis can detect slow and time-variable deformation with high precision, typically at a rate of a few millimeters per year. For example, (Lohman and Simons, 2005) illustrate the effectiveness of InSAR in locating shallow earthquakes that may be too small or far away to be accurately located by traditional seismic methods was demonstrated by (Lohman and Simons, 2005).

The Centre for the Observation and Modelling of Earthquakes, Volcanoes, and Techniques (COMET) is leading a project called "Looking Inside the Continents from Space" (LiCS), which aims to observe and study the Earth's interior using satellite-based remote sensing techniques. The primary objective of the LiCS project is to enhance our understanding of the deformation of continents at various both time and geographical scales. A key focus of

the project is to analyze the earthquake deformation cycle and gain insights into how earthquake risk is dispersed over time and space (Wegmüller et al., 2015; Werner et al., 2000). To facilitate the project's objectives, a free-source package for SAR interferometry time series analysis, called LiCSBAS, has been created and implemented utilizing the automated sentinel 1 InSAR procedure (COMET_LiCSAR). The use of LiCSBAS enables the utilization of immediate on the COMET-LiCS web platform released goods (Morishita et al., 2020).

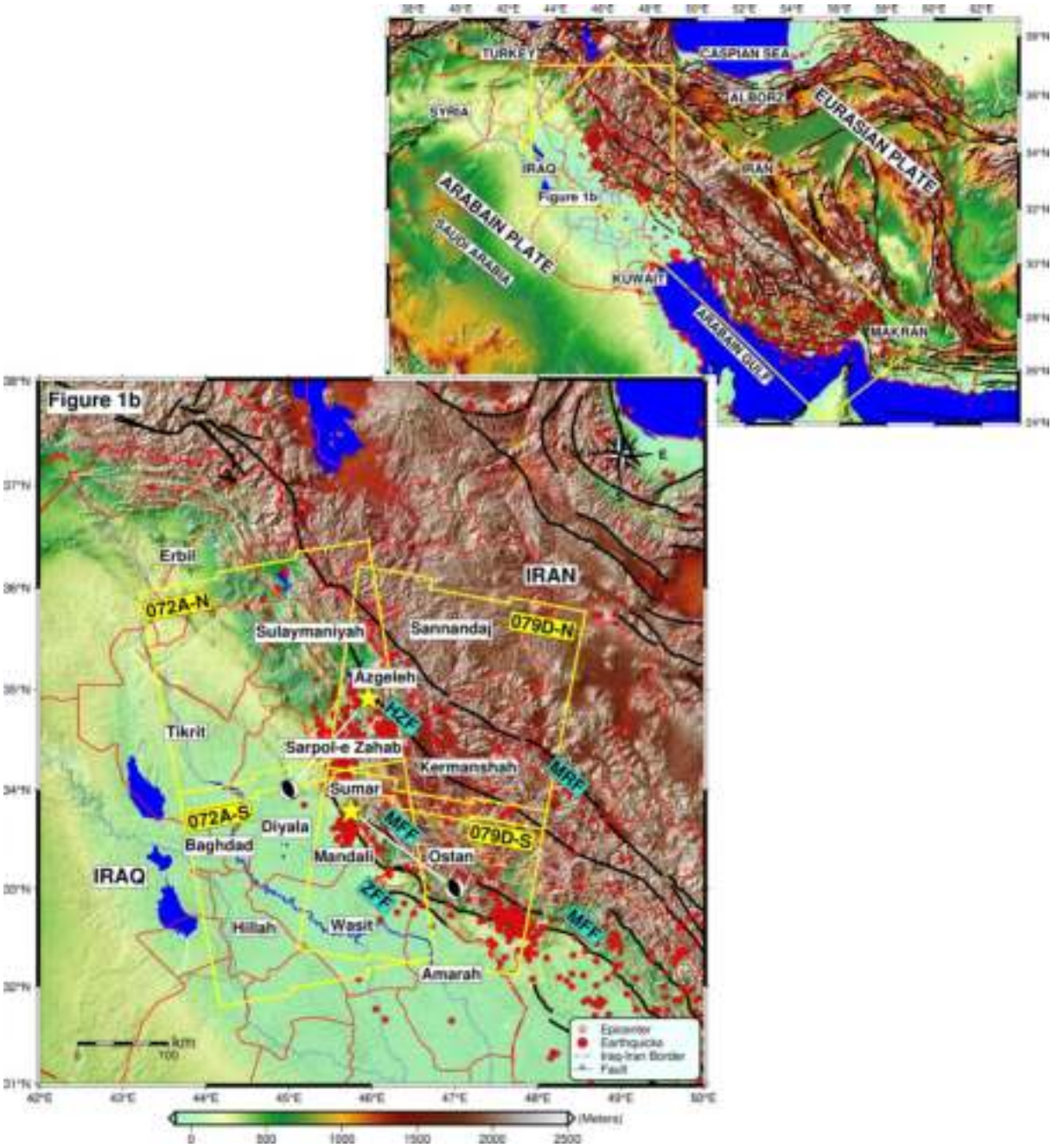

Fig. 1. (a) The tectonic setting of the Zagros mountains. The Global Centroid-Moment-Tenser (GCMT) database displays earthquakes with red dots that are greater than magnitude 4.5. (2014-2022), and the black line shows a major active fault (MRF=Main Recent Fault: HZF=High Zagros Fault: MFF=Mountain Front Fault: ZFF= Zagros Foredeep Fault). The red line shows the Iraq-Iran borders. The location of the study area shown in (b), the shaded relief map of the study area is located between longitude 43°30'00" – 48°30'00" and latitude 31°50'00" – 36°30'00". The yellow rectangle indicates the boundaries of the sentinel interferogram that was utilized to study the 2017 Sarpolzahzb mainshock, and the 2018 Mandali mainshock and yellow stars show the epicenter earthquake.

On November 12, 2017, at 18:18 UTC, a powerful earthquake measuring 7.3 Mw struck approximately 50 km north of Sarpol-e Zahab city. The epicenter of the earthquake was a few kilometers east of the Iraqi border, close to the Iranian town of Ezgeleh, with an aperture depth of around 22 km. The earthquake was the largest one to be recorded in the area since instrumentation records began inside the Lurestan Arc of the ZFTB, following a shallow east-dipping reversal fault with dextral components. Several aftershocks, even the Mw 5.9 earthquake that occurred on August 25, 2018, and the November 25, 2018, Mw 6.3 earthquake, occurred in the sedimentary cover following the mainshock. The earthquake resulted in the deaths of over 600 people and injuries to more than 8,000, while over 12,000 buildings were destroyed, leading to significant economic losses (Vajedian et al., 2018b).

The activity that followed the earthquake in the Ezgeleh-Sarpol-e Zahab fault plane characterizes the string of occurrences close to Mandali-Sumar as of January 11, 2018. This includes a main shock Mw 5.5 earthquake at 06:59 UTC, three aftershocks of Mw 5.2-5.3 Mw occurring quickly, and over 5 km later at 07:14, 07:21, and 08:00 (Nissen et al., 2019).

Numerous research studies have examined the source characteristics of the earthquake in question and its impact on the surrounding area through the analysis of seismic, geodetic, and: (Abdulnaby, Mahdi, Al-Shukri, et al., 2014; Abdulnaby, Mahdi, Numan, et al., 2014; Abdulnaby et al., 2016) investigated the side effect of the earthquake in this area. In their study published (Luo and Chen, 2016; Vajedian et al., 2018a; Washaya and Balz, 2018), Feng and colleagues employed SAR data from the period of the earthquake and its immediate aftermath to estimate the shape of the fault and the distribution of slip along it.

This paper aims to create a map of neotectonics deformation of the ground along the Iraq-Iran borders from 2014 to 2022 and detect fault activity because of the earthquakes that occurred on November 12 and January 11, 2018, using inSAR techniques and confirmation on the processing, dissection, and implementation of Sentinel-1 data supported by field, and tectonic information.

Materials and Methods

1. Data

In this study, 1285 C-band (with a wavelength of 5.6) Copernicus Sentinel-1 A/B interferometric wide-swath scenes were used across two ascending tracks (072A, 072A) and two descending tracks (072A, 072A) associated with the Mw 7.3 Sarpol-Zahab earthquake on November 12, 2017, and the Mw 5.5 earthquake on January 11, 2018. Interferograms were formed between each acquisition to create a reduction network with minimized temporal baseline averaging nine years from 2014 to 2022, resulting in a total of 6526 interferograms. A long temporal baseline interferogram was produced between each period to decrease decorrelation, and a total of 371 interferograms were removed as they could not be generated correctly due to processing errors.

The interferogram was generated using LiCSAR, which is a combination of sophisticated tools and algorithms that utilize the GAMMA SAR software, and it was filtered using an adaptive phase filter (Morishita, 2021; Werner et al., 2000). Table 1 gives specifics about the SAR pictures that were used for the InSAR time series study. To correct the effect of topography on the interferometric phase measurements, the 1 arc-second-SRTM DEM is used to remove topographic contributions to the phased return (Farr et al., 2007). The method known

as statistical-cost network flow is used to process the interferograms (SNAPHU) to unwrap them in two dimensions. Before this, the interferograms are multi-looked by 20 in range and 4 in azimuth, resulting in a ground resolution of 46x56 meters. Additionally, the data is down-sampled to 100x100 meter pixels outside of GAMMA. By Observing the Landscape with Progressive Scans (TOPS) mode, a set of predetermined frames is used for processing the images, with each frame comprising an average of 13 bursts obtained from the three sub-swaths (Motagh et al., 2014).

The effect of atmospheric variables on observed displacement signals is minimized to some extent by utilizing the paradigm of iterative troposphere decomposition used in the Generic Atmospheric Correction Online Service for InSAR (GACOS) (Yu et al., 2018; Yu et al., 2017).

Table 1: The length of time and the total amount of processed Information utilized in this study for each track.

Tracks	Starting	Ending	Duration	Number of Scenes	Number of Interferograms	Number of Interferograms Used	GACOS
072A-N	2014/10/10	2022/10/28	7.8	363	2163	2050	335
072A-S	2014/12/09	2022/10/28	8	356	1930	1850	334
079D-N	2014/11/28	2022/10/29	8.2	285	1343	1245	264
079D-S	2014/11/04	2022/10/29	7.8	281	1090	1010	261

2. Time Series Analysis

We employ LiCSBAS, a program for analyzing small-baseline time series, to extract cumulative line-of-sight displacements and average velocities from our interferograms (Morishita, 2021; Morishita et al., 2020). we will provide a detailed explanation of the software summarized below. the processing method is divided into three stages. firstly, pre-processed the Sentinel-1 images to create an unwrapping interferogram (UNW) and coherence. To start processing the data in this study, LiCSBAS first downloads LiCSAR products covering the study area (Steps 0-1) then, Geo TIFF files are transformed into a single processing floating-point format devoid of heading details (Steps 0-2).

Atmospheric noise is one of the most common sources of pollution in the interferograms, which is caused when radar waves pass through the troposphere (Parker et al., 2015; Zebker et al., 1997), some of these waves interact with air molecules, causing them to change direction and spread in different directions, while others are absorbed by the atmosphere. Radar waves can also interact with rain, snow, fog, and other materials in the air, causing the waves to reflect and scatter in different directions. As a result, all these factors can cause delays in the speed of the waves, which can lead to problems in understanding the return radar's wave (Hamlyn et al., 2018). Standard time-series analysis algorithms employ temporal-spatial filtering to distinguish between spatially correlated noise and signal distortions (Bekaert et al., 2015; Osmanoğlu et al., 2016). This technique assumes that the noise component is not dependent on time, but this assumption is not always valid since noise can be time-dependent in some instances. As a result, it is crucial to consider the potential impact of time-dependent noise components when utilizing these algorithms.

To mitigate the noise in the troposphere, which can reach 10 cm or more in interferograms (Yu et al., 2018), we utilize the online Atmospheric Correction Service for InSAR (GACOS) as shown in Fig.2. This service provides high-precision data for the delay that occurs in the

atmosphere, as well as the hydrostatic and humidity conditions every six hours, Provided by the European Centre for Medium-Range Weather Forecasts (ECMWF). They may be extrapolated to any SAR acquisition time in between by using this data. Then, Projecting the necessary delay values onto the LOS of the satellite, which then subtracts from the interference stacking (Kirui et al., 2021) (Steps 0-3).

Then we applied it to mask the area in the stack of unwrapped interferogram data, the mask is effective when the unwrapped data include an area that contains many unwrapping errors and is not of interest (step 0-4). Clip unwrapped data, clipping can reduce the data size and processing faster and improve the results of step 12 (loop closure) (Steps 0-5).

secondly, this stage involves six steps for computing the displacement rate. The first step is to assess the quality of the input data, both good and bad, based on statistics derived from the processing, including the percentage of valid pixels and the coherence values resulting from the interferometric process. Then, all the bad data are removed from the processing depending on the pre-selected phase unwrapping values of 0.3 and 0.05. If the phase values in a pixel are below these pre-selected values, it is removed from processing. By taking this action, it is ensured that only high-quality data is used are used in the subsequent calculations.

In step two, we used a network of interferograms and lop phase closers for each interferogram image's redundancy to correct and identify unwrapping phase inaccuracy. after equation 1 (Biggs et al., 2007).

$$\boldsymbol{\phi 123 = \phi 12 + \phi 23 + \phi 13} \quad (1)$$

The interferograms Φ12, Φ23, and Φ13 are created by processing SAR images Φ1, Φ2, and Φ3. Ideally, if all three interferograms are error-free, the loop phase should be nearly zero, although slight deviations can occur due to factors such as multi-looking, filtering, and variations in soil moisture (Zan et al., 2015). However, if one or more interferograms include unwrapping mistakes, the loop phase is typically very close to a multiple of 2π. This behavior can help identify areas of the interferograms where unwrapping errors have occurred and guide the selection of appropriate data processing techniques to improve the accuracy of the results.

Bad interferograms can be identified and removed by calculating the Root Mean Square (RMS) for a single loop interferogram and setting a threshold of 1.5 rad (Biggs et al., 2007). In the third step, a Small Baseline (SB) inversion is applied to the network of interferograms to estimate the surface pixel velocity over time using the time series of displacement data. This technique helps to determine the small changes in displacement that occur between the interferometric pairs, enabling more exact calculations of the surface feature's velocity (Yu et al., 2018).

The unwrapped interferogram is considered the sum of corresponding successive incremental displacement (Doin et al., 2011). To determine the mean displacement velocity, the incremental displacements are summed up to calculate the cumulative displacements for each acquisition. A least squares method is then used to transform the cumulative displacements into the mean displacement velocity. The best pairs of scenes were selected to form the network of both the descending and ascending tracks' final interferograms. (Agram et al., 2012).

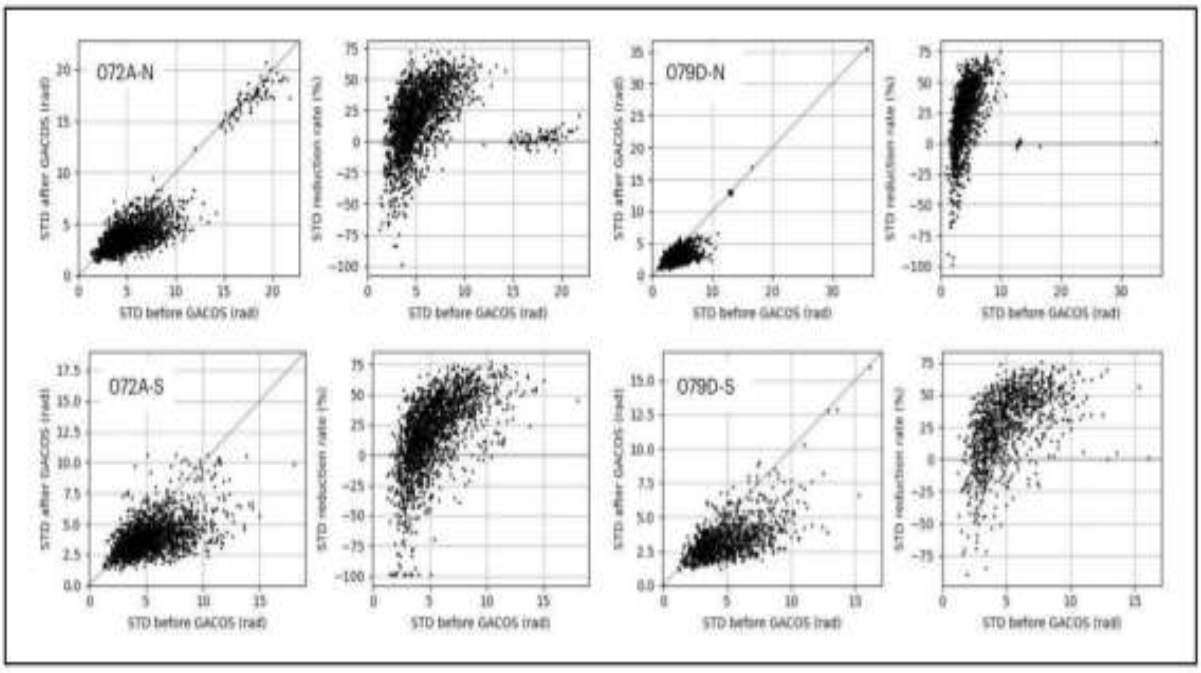

Fig.2. Applying the (GACOS) correction causes a shift in the total standard deviation (SD) of each interferogram's pixels. Below the black dashed line, black dots are indicating a reduction in interferogram noise because of the use of the atmospheric model. An interferogram is represented by each black dot. The bottom right of each sub-panel contains the percentage of interferograms for each frame that exhibit a reduction in SD. The recognizable high SD clusters seen in 072A-N and 072D-S are related to the Mw 7.3 and Mw5.5 earthquakes.

The NSBAS technique is used to invert the original interferograms to acquire time series displacement. In this phase, the choice of a reliable reference point, and linear displacement behavior is presumed to occur over time. To choose The reference point is established as the RMS of each phase loop for each pixel, and the reference point is chosen to be the pixel with the lowest RMS (López-Quiroz et al., 2009).

In the four-step, to calculate the velocity standard deviation, we utilize the bootstrap method (Cignetti et al., 2016) with a sampling rate of 100. However, some pixels may still be unstable despite the network's progress in earlier stages (Efron and Tibshirani, 1986). To address this, a mask composed of the pixels is subjected to several noise indicators in five steps to identify defective pixels (Morishita et al., 2020). When the value of any noise indicator for a specific pixel exceeds a certain threshold, that pixel is flagged and excluded from the analysis. Finally, in six steps, a spatiotemporal filter is employed to remove the orbital error, residual ionospheric noise, and tropospheric noise from the displacement time series (Bell et al., 2008; Hoffmann et al., 2001; Hooper et al., 2012).

3. Sentinel-1 Data Decomposition into 2D Displacement Rates

Line of sight (LOS) measurements, which are one-dimensional displacements, are taken by radar satellites. The satellite will notice that, depending on the direction of movement, the distance between itself and the object either grows or reduces if the object has moved. Since LOS measurements frequently include both vertical and horizontal components of movement, they can be difficult to interpret. However, ascending orbits (satellites traveling from south to north) and descending orbits (satellites traveling from north to south) are two examples of distinct viewing perspectives that can be used to observe the same location to acquire information on multi-directional ground movement (Braun, 2021).

Line-of-sight (LOS) data can be used to produce a standardized point grid that can be used to extrapolate the true vertical and east-west horizontal vectors using the basic vector geometry method, as illustrated in Fig.3. The radar satellite follows an almost polar orbit and captures images using right-looking geometry, with the radar beam facing either east or west. This means that the satellite can detect vertical and east-west ground movements, but it is unable to distinguish between the north and southward movement of the ground due to the SAR satellite's orbit being close to the pole (Shi et al., 2020). Therefore, to carry out the analyses in these studies, the LOS velocity fields generated from both ascending and descending tracks of Sentinel-1 images were decomposed into their respective horizontal and vertical components. This decomposition was accomplished by applying a 2D decomposition equation (Equation 2) whose local incidence angle of the satellite image in the azimuth direction is taken into consideration (Fan et al., 2021).

$$\boldsymbol{V_{LOS} = V_V\, Cos\, \theta - (V_e\, Cos\, \alpha - V_n\, Sin\, \alpha) Sin\theta} \quad (2)$$

Three unknowns are present in the equation for determining ground motion from line-of-sight velocity (VLOS), local radar incidence angle (Θ), azimuth of the satellite heading vector (α), and a vector denoting east, north, and vertical motion ([Ve Vn Vv]). To solve for these unknowns, we can employ two observational constraints, namely the rising and descending line-of-sight velocities.

The form of Equation 2 is altered when working with spaceborne synthetic aperture radar (SAR) systems due to their near-polar orbits, into the following form:

$$\boldsymbol{V_{LOS} = V_V\, Cos\, \theta - V_e\, Cos\, \alpha\, Sin\, \theta} \quad (3)$$

To solve Equation 3, it is necessary to have at least two separate measurements from both ascending and descending orbits for each pixel. These measurements can be utilized to create a matrix in the following form, as shown in Equation 4 (Pawluszek-Filipiak and Borkowski, 2020).

$$\begin{pmatrix} V^a_{LOS} \\ V^d_{LOS} \end{pmatrix} = \begin{pmatrix} COS\,\theta^a & -COS\,\alpha^a & sin\theta^a \\ COS\,\theta^d & -sin\alpha^d & sin\theta^d \end{pmatrix} \begin{pmatrix} V_v \\ V_{EW} \end{pmatrix} \quad (4)$$

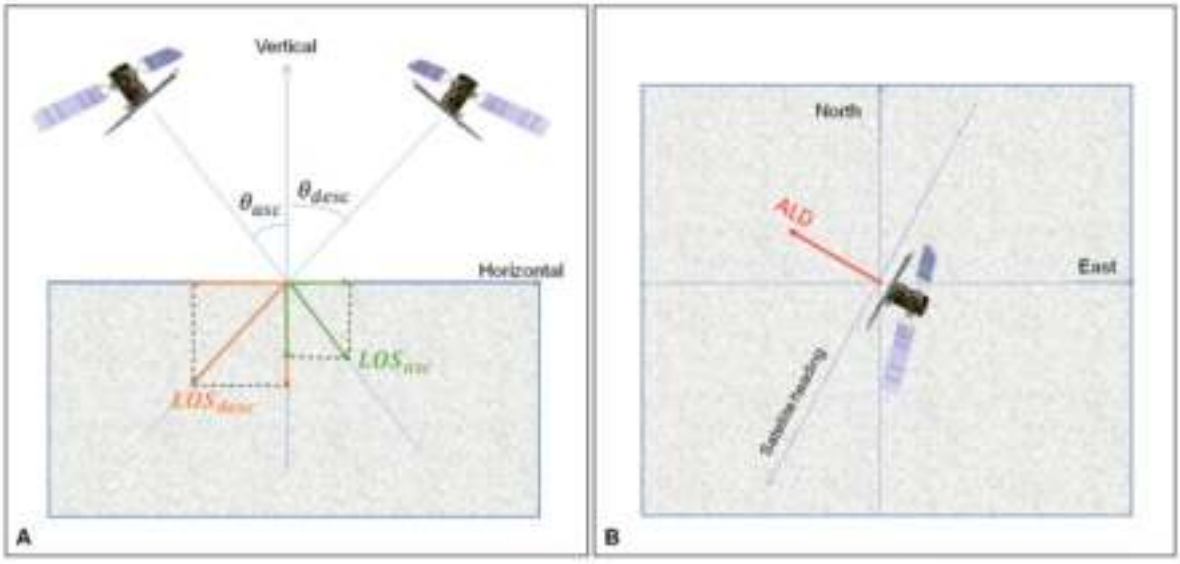

Fig. 3. Horizontal components, ascent and descent, and azimuth look direction for descent orbit pass are shown in (A) and (B), respectively (Delgado Blasco et al., 2019).

The superscripts "a" and "d" in the matrix of Equation 4 refer to the ascending and descending geometries, respectively. This method of combining measurements from both ascending and descending orbits enables the determination of ground motion in different directions. The SAR sensors used in this study provide a range of temporal sampling of ground motion, allowing coverage of various periods. Additionally, the SAR sensors employed in this study have different spatial resolutions, which could potentially influence the results of the decomposition process (Pawluszek-Filipiak and Borkowski, 2020). In this study, the velocity maps obtained from both ascending and descending orbits of the S1 data had the same temporal and spatial resolution. As a result, Equation (4) was applied to both maps. Before inverting the equation to determine the rates of east-west and vertical displacement, the geocoded line-of-sight (LOS) displacement rates obtained from S1 NSBAS were extrapolated onto the same geographic grid points.

Results and Discussion

1. Line-of-Sight Along the Co-Seismic Deformation

To obtain the co-seismic displacement, the NSBAS method, Sentinel-1 sensor data obtained from both ascending and descending orbits were subjected to the same processing, as stated in Section 2.2. This approach enabled the computation of the line-of-sight (LOS) direction displacement caused by the earthquake event. By using data from both orbits, a more comprehensive picture of the co-seismic displacement can be obtained, to identify and understand how the earthquakes that occurred during the period (2014-2022) affected the land in the area and this makes it possible to analyze how the surface change before and after earthquakes. Assuming that the altitude of a satellite is constant, any variation in the elevation of the Earth's surface can serve as an indication of directional movement resulting from tectonic activity. When the elevation increases, it signifies movement toward the radar, whereas a decrease in elevation indicates movement away from the radar. Fig.4 and 5, show the average annual displacement along the Line of Sight (LOS) of the satellite and the coseismic deformations patterns obtained from TOPS interferometry measurements for two earthquakes that occurred in the area.

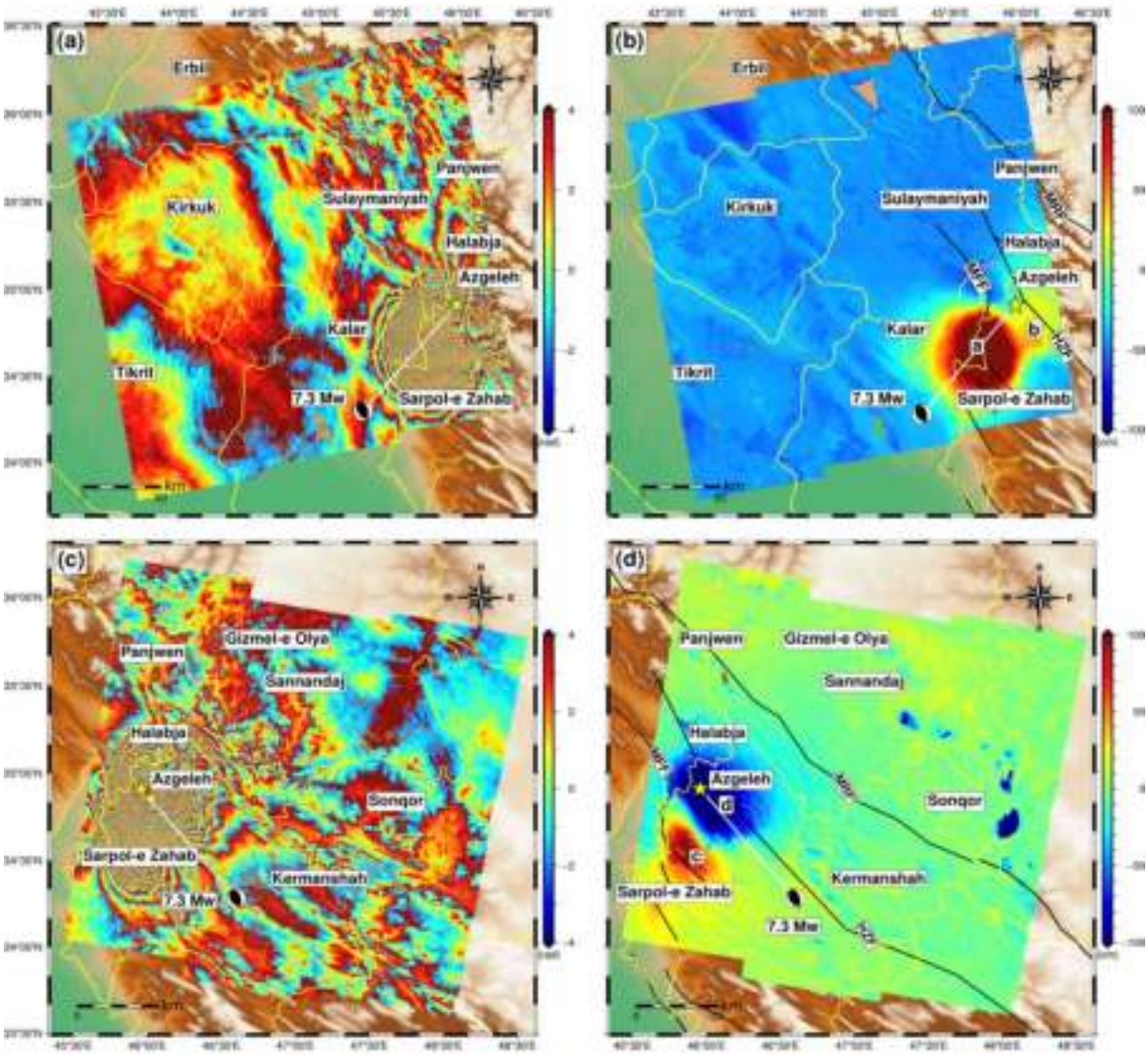

Fig.4. The deformation caused by an earthquake that was observed in Sentinel-1 Synthetic Aperture Radar (SAR) images. (a-c) illustrative of the co-seismic deformation differential interferograms, (b, d) shows the line-of-sight co-seismic deformations. The yellow star represents the epicenter of the mainshock. The color cycle, which goes from blue to red, corresponds to half the wavelength of radar (which is 0.028 meters) in the direction of the (LOS).

The first earthquake, which was the Sarpol Zahab earthquake, occurred on 12 November 2017. The epicenter of the main shock was located just a few kilometers north of the city of Ezgeleh, which is situated west of Iran and along the Iraqi border. This earthquake was exceptionally strong and resulted in extensive damage to the surrounding areas, with a magnitude of around 7.3. Subsequently, a series of destructive aftershocks followed the shock as the 25 August 2018 5.9 Mw event and the 25 November 2018 6.3 Mw. Co-seismic deformation in the line-of-sight direction may be seen in both the ascending and descending tracks. In track (b), an uplift area that is almost circular is evident, with a maximum deformation of approximately 90 cm in the line-of-sight direction. On the other hand, track (d) shows a double elliptical pattern of deformation, with the maximum uplift and subsidence measuring 60 cm and 40 cm, respectively, as depicted in Fig.4. In both the ascending and descending tracks, a distinct co-seismic signal in the NNW direction is evident, which aligns with the USGS-

provided strike angle direction and is parallel to the MFF and HZF. The observed consistent deformation pattern during co-seismic deformation implies that the fault did not rupture to the surface. The deformation areas for the ascending and descending tracks cover approximately 70 km^2 and 90 km^2, respectively.

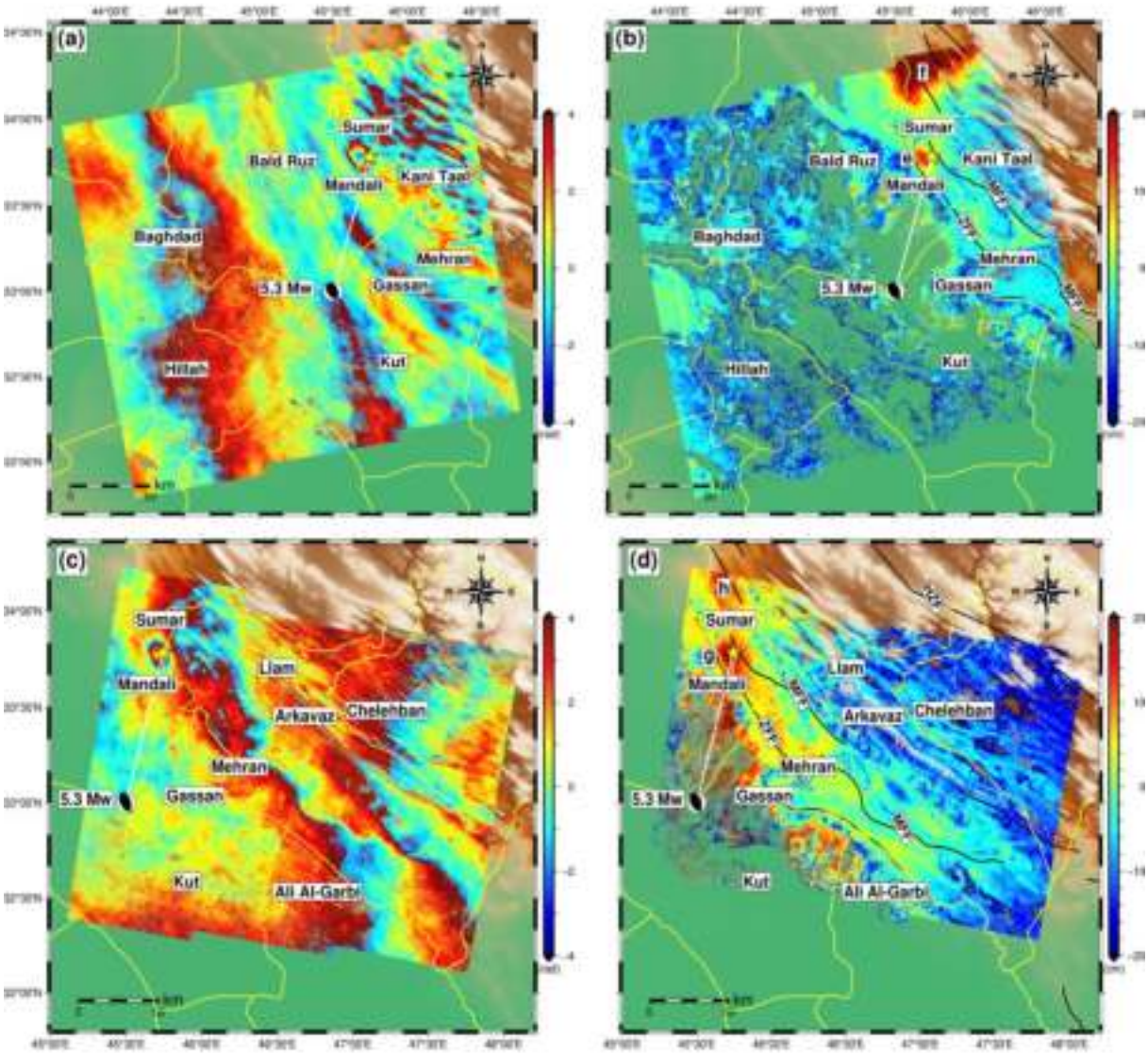

Fig.5. The deformation caused by an earthquake that was observed in Sentinel-1 Synthetic Aperture Radar (SAR) images. (a-c) illustrative of the co-seismic deformation differential interferograms, (b, d) shows the line-of-sight co-seismic deformations. The yellow star represents the epicenter of the mainshock. The color cycle, which goes from blue to red, corresponds to half the wavelength of radar (which is 0.028 meters) in the direction of the line of sight.

The second is the Mandili-Sumar earthquake, which occurred on January 11, 2018, and is characterized by activity following the earthquake surrounding the Ezgeleh-Sarpol-e Zahab fault plane. This includes a main shock Mw ~5.5 earthquake at 06:59 UTC followed quickly and over 5 km by three aftershocks of 5.2–5.3 Mw at 07:14, 07:21, and 08:00 (Nissen et al., 2019). The interferograms show a roughly oriented NNW-SSE deformation fringe that had offsets of 21 cm in track (b) and 17.6 cm in track (d) orbits towards the satellite shown in Fig.5a and b. The fringe closely matches the Zagros Foredeep Fault's dipping point's location and

direction. The deformation region's size is approximately 27 km^2 for ascending orbits and 23 km^2 for descending orbits.

The InSAR technique enables visualization of ground deformation through changes in fringe colors, with gradual changes indicating moderate deformation and abrupt changes indicating severe deformation. Using a red-to-blue color cycle, an interferogram can display the degree and pattern of deformation. Each fringe, or cycle of color, is equivalent to a change in the satellite-to-ground distance equal to one-half of the radar wavelength (Weike and Goulin, 2013). Furthermore, the fringe colors also display the values of ground deformation, which can be either positive or negative. These values can be expressed either in radians (ranging from π to -π) or in metric units, which are equivalent to the wavelength of the radar satellite used, as shown in Fig.6. For example, since the wavelength of the S-1 satellite is approximately 5.6 cm, the fringe colors would represent deformation values ranging from 2.8 cm to -2.8 cm. Calculating the relative displacement between two points within the radar's field of view involves a multiple of the fringes separating them by half the wavelength. The fringes in the pattern are color-coded in red, yellow, and blue, with the center indicating the reference point. The presence of red-yellow-blue fringes demonstrates that the target has moved away from the satellite, while the presence of blue-yellow-red fringes in reverse order indicates that the target has moved toward the satellite.

The target travels away from the satellite during subsidence or a westward move and towards the satellite, during an uplift or an eastward move if the satellite is moving from the North to the South (descending orbit). On the contrary, subsidence or an eastward move away from the satellite, while blue-yellow-red color in the opposite order indicates that the target has moved toward the satellite.

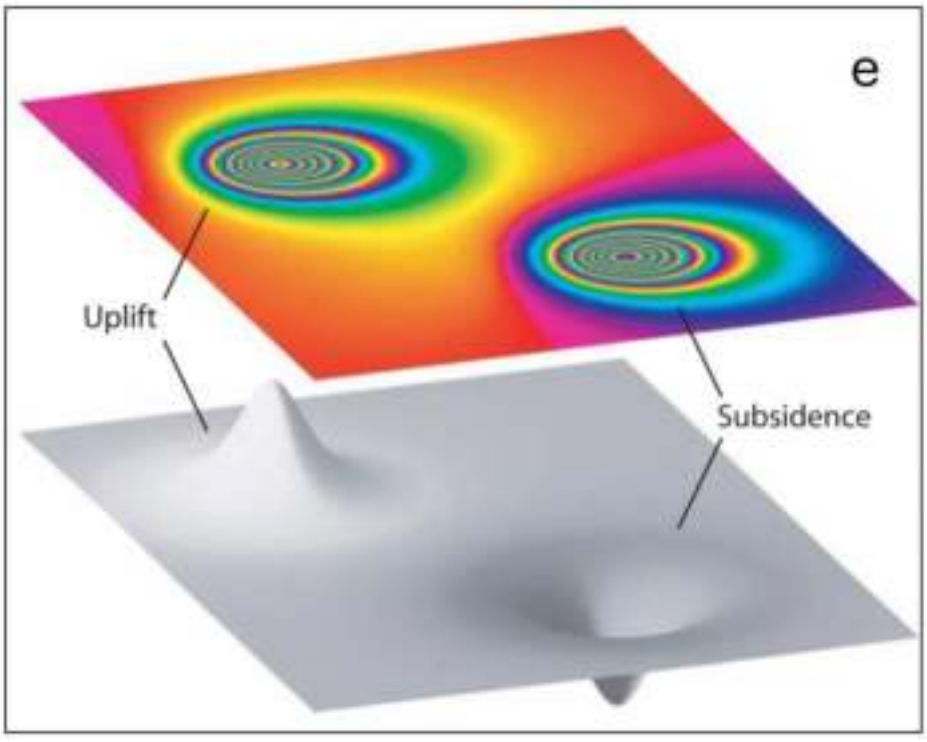

Fig.6. Each fringe in a topography-removed interferogram can be represented by a color band ranging from red to violet.

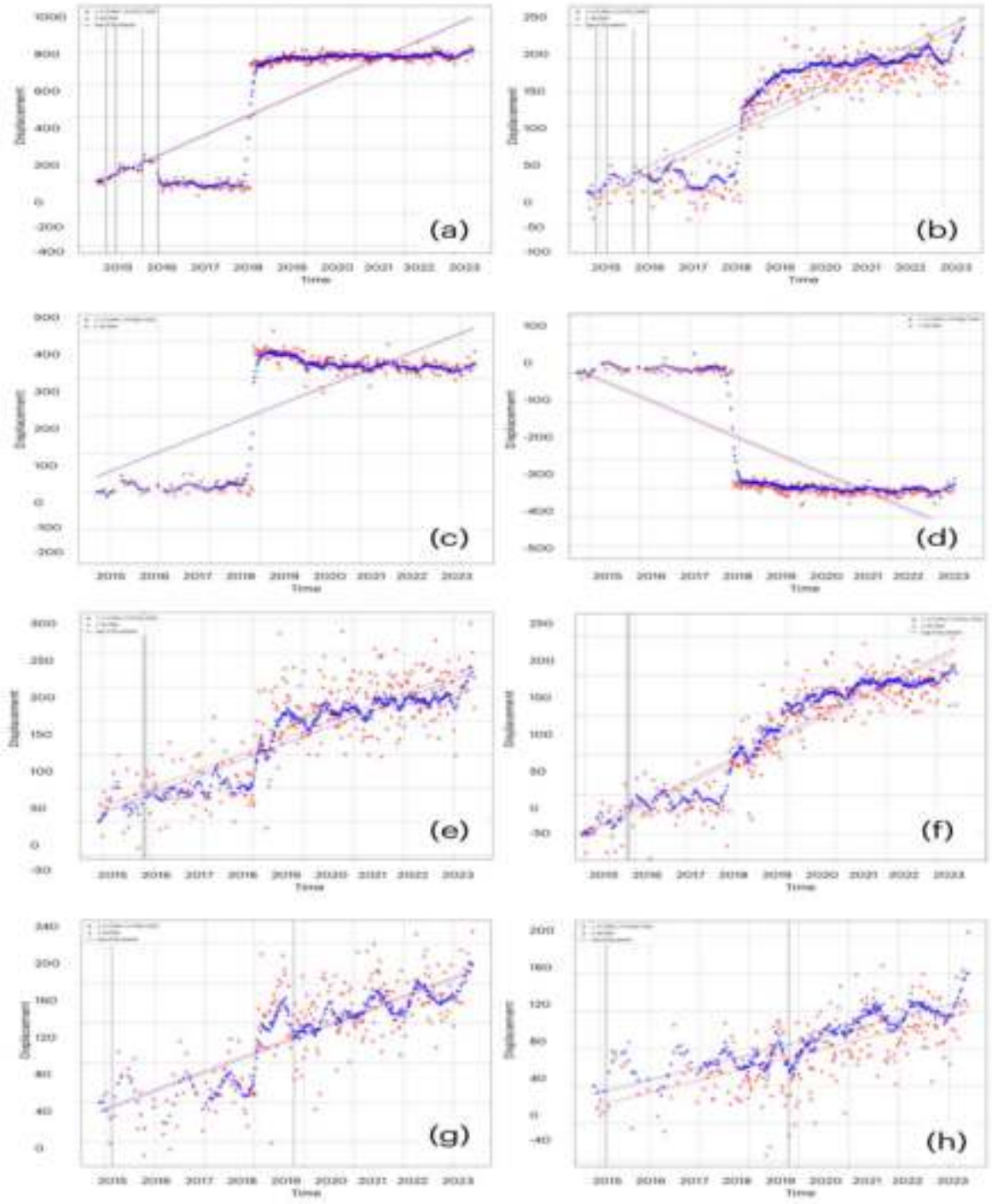

Fig.7. Time series displacement at the selected reference point. (a, b, c, d) from Fig.5a and b, respectively. (e, f, g, h) from Fig.6a and b, respectively.

According to the details in Table 2. We have selected two reference points in areas of high deformation for each path, as shown in Fig. 4 and 5, to calculate the change in displacement rate that occurred in the area due to fault movement and earthquakes over time. Fig.7. illustrates the displacement change at each point over time.

From the chosen points (a, b, c, d) for the Sarpol area, as shown in Fig.4b and d, we can observe a slight rise in ground level from the beginning of 2014 until the end of 2017. This

relative rise can be attributed to small earthquakes. However, after the earthquake that occurred in November 2017 with a magnitude of about 7.3, the ground level rose significantly, and the highest point in the region reached a rate of 800 mm at point a. We also observe the continuity of the relative height after the earthquake occurred in the region. At point d, we can observe that the area northeast of the epicenter of the earthquake has subsided, and this can be attributed to the movement of the fault, as well as to the subsidence of one plate under the other due to the force of the collision. The total rate of subsidence was about 400 mm, and we can also observe the continuity of the relative subsidence in the region.

Regarding the points (e, f, g, h) that were chosen for the Mandali region, as shown in Fig.5b and d. we can also observe a relative rise in the Mandali region until 2018. After the occurrence of a 5.3-degree earthquake, the rise was small compared to the previous earthquake that occurred in Sarpol at points (a, b, c). The highest point reached by the region was 250 mm. We can also observe from the graph that the rise continues every year in this region due to the continued occurrence of small earthquakes there. Additionally, there is no subsidence in the Mandali region, as observed in the northeast of Sarpol. This may be attributed to the occurrence of an earthquake due to the movement of the fault without a collision between the two plates.

Table 2: Maximum cumulative LOS displacement at the reference point.

Area	Ascending Reference point Lat – long		Descending Reference point Lat -long	
	a	b	c	d
Sarpol-e Zahab	34.624-45.724	34.659-45.867	34.525-45.832	34.846-46.049
	800 mm	240 mm	430 mm	-400 mm
	e	f	g	h
Mindali-Sumer	34.45.798-45.798	34.165-45.587	33.781-45.713	34.092-45.656
	250 mm	210 mm	220 mm	185 mm

2. The Rates of Vertical and Horizontal Displacement

The movement and deformation that occurs after a major earthquake are due to the redistribution of stress caused by the earthquake in the host rocks. It is important to conduct ongoing research and observe these changes using geodetic techniques to better understand how earthquakes are formed and how rocks react to variations in stress. By studying post-seismic deformation, we can learn more about the procedures used to create earthquakes and better comprehend the specific ways that rocks respond to stress changes after an earthquake. By the process outlined in Section 2.3, we obtained the 2D displacement data for the Line-Of-Sight (LOS) and along-track directions using Sentinel-1 satellite data for both ascending and descending tracks. These data were then used to estimate the cumulative horizontal (EW) and vertical (UD) deformation that occurred in the region.

The co-seismic deformation field produced using the data is presented in Fig.8. It was observed that the post-earthquake deformation pattern in the Up-Down direction occurred mainly towards the southwest of the epicenter within 350 days after the mainshock, which is distinct from the co-seismic deformation pattern. The maximum uplift and subsidence displacement were found to be 100 cm and 35 cm, respectively, in the Sarpol area, whereas the maximum uplift in Mandali was 20 mm. Compared to the northeastern patch, the southwestern patch underwent greater after-slip. The two main displacement zones also showed westward movement in the East-West direction, with Sarpol experiencing a maximum westward movement of approximately 20 cm and Mandali experiencing a maximum westward movement of about 5 cm. During the Iran earthquake, the subduction zones shallowly sloping front edge experienced abrupt rupture. Consequently, a zone of uplift was created in front of the block

near MFF, while a zone of subsidence formed at the opposite end due to tension the hanging wall experienced significant elevation and subsidence because of the earthquake.

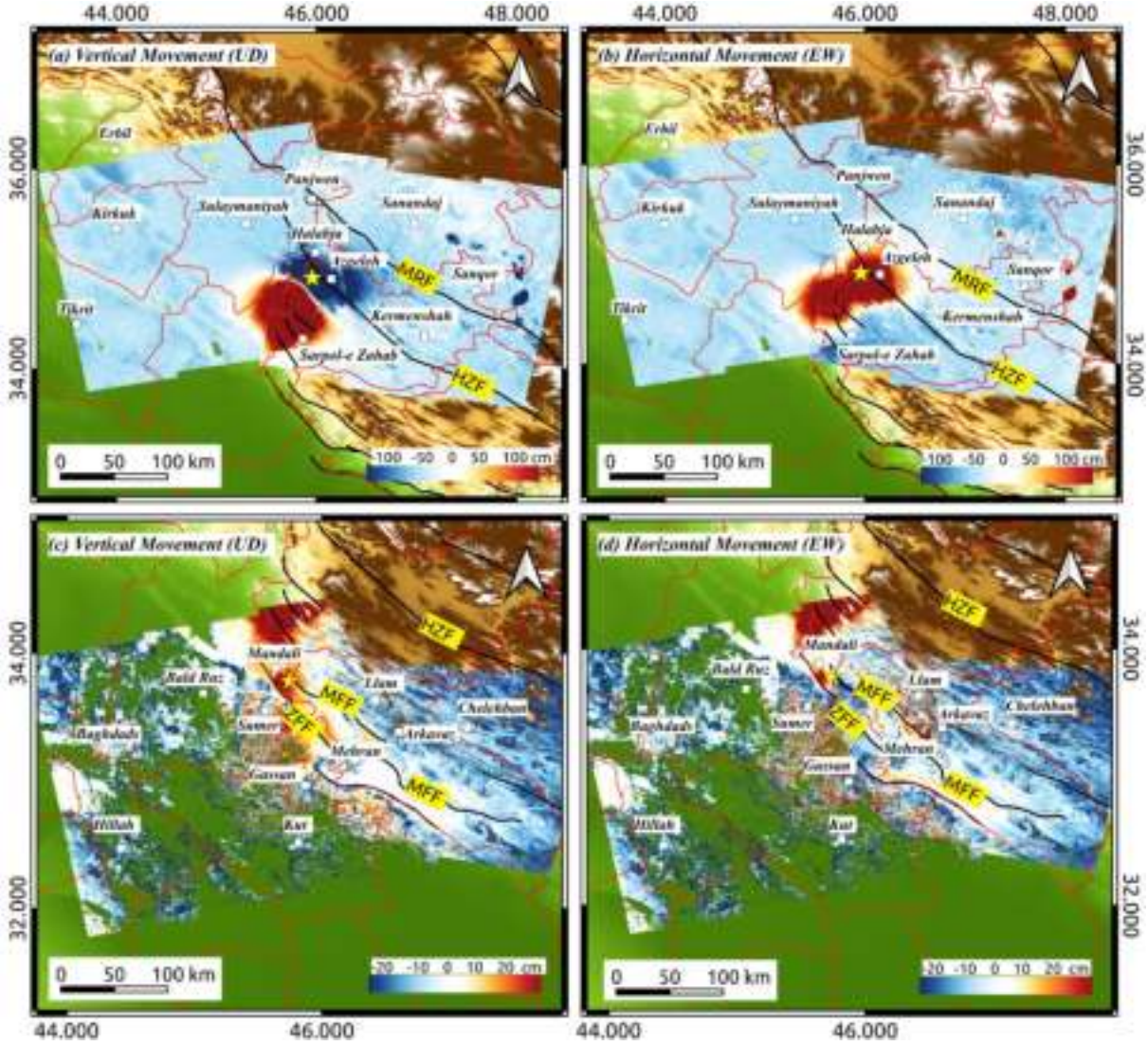

Fig.8. By employing a 2D decomposition technique on a long-up-track and across-track observation, two sets of time series data can be obtained. These data sets are represented by (a, b) and (c, d) and correspond to the cumulative up-down (UD) deformations and the cumulative horizontal east-west deformations, respectively. In the given context, the active fault is depicted as a black line, and the epicenter of the earthquake is represented by a yellow star. The positive and negative values in the time series data indicate uplift/subsidence and eastward/westward movement, respectively.

Conclusions

The InSAR method was employed in this paper to study the neotectonics deformation along the Iraq-Iran border. After analyzing the Sentinel-1 SAR images from both the ascending and descending tracks, we have reached the following conclusion:

1. Between 2017 and 2018, the seismic events that took place in northeastern Iraq included the most significant earthquake ever documented in the Zagros region. The deformation caused by the earthquake was dispersed across complex fault patterns that followed trends in the East-West, Northeast-Southwest, and North-Northwest to South-Southeast directions.

2. For obtaining the time series of 2D post-seismic deformation, the NSBAS technique was employed. The findings indicate a significant deformation surface in both the Up-Down and East-West directions. The uplift phenomenon was observed in the southwestern region, while subsidence occurred in the northeastern area of the epicenter. Moreover, in the East-West directions, there was a noticeable westward motion.

3. The earthquake originated in the vicinity of Ezgeleh and propagated southward, causing the most severe damage near Sarpol-Zahab. The initial aftershocks were concentrated at the boundaries of the mainshock slip region, primarily in the southern and western regions. Additionally, there was a group of aftershocks near Mandali in Iraq, which is situated approximately 80 km to the south of the earthquake epicenter.

4. There is always a greater vertical displacement than a horizontal displacement because the dominant force in the area is the compressive force due to the collision process. The Sarpol earthquake serves as an example of how earthquakes with higher magnitudes and stronger forces can result in a larger surface deformation area.

5. Fig. 9, illustrates the ultimate deformation changes caused by earthquakes along the Iraq-Iran borders.

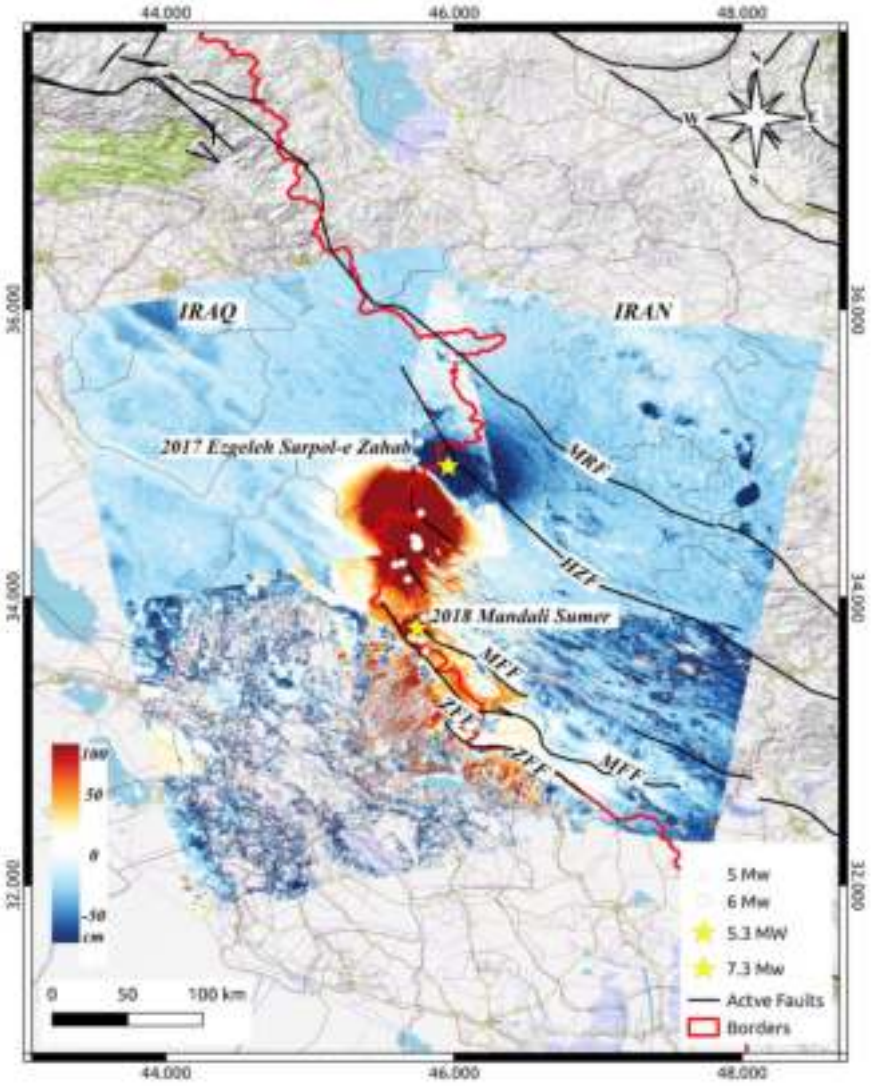

Fig.9. The final displacement that occurred along the Iraq-Iran border from 2014 to 2022 by collecting four tracks covering the study area.

Acknowledgments

Our appreciation goes to the appreciation of the European Space Agency's free provision of Sentinel-1A data. Additionally, we extend our gratitude to the reviewers and the editor for their valuable feedback and recommendations that will greatly enhance the quality of this paper.

References

Abdulnaby, W., Mahdi, H., Al-Shukri, H. and Numan, N.M., 2014. Stress patterns in northern Iraq and surrounding regions from formal stress inversion of earthquake focal mechanism solutions, pure and applied geophysics, 171, pp. 2137-2153, https://doi.org/10.1007/s00024-014-0823-x.

Abdulnaby, W., Mahdi, H., Numan, N.M. and Al-Shukri, H., 2014. Seismotectonics of the bitlis–Zagros fold and thrust belt in northern Iraq and surrounding regions from moment tensor analysis. Pure and applied geophysics, 171, pp.1237-1250. https://doi.org/10.1007/s00024-013-0688-4

Abdulnaby, W.,Mahdi, M., Al-Mohmed, R. and Mahdi, H.H., 2016. Seismotectonic of badra-amarah fault, Iraq−Iran border. iosr journal of applied geology and geophysics (iosr-jagg), 4(3), pp.27-33. https://doi.org/10.1007/s40808-016-0201-z

Abdulnaby, W., Motaghi, K., Shabanian, E., Mahdi, H., Al-Shukri, H. and Gök, R., 2020. Crustal structure of the mesopotamian plain, east of Iraq. Tectonics, 39(11), pp1-16. https://doi.org/10.1029/2020tc006225

Agram, P.S., Jolivet, R. and Simons, M., 2012. Generic insar analysis toolbox (giant) user guide. https://doi.org/10.1002/2013eo070001

Bekaert, D.P.S., Walters, R.J., Wright, T.J., Hooper, A.J. and Parker, D.J., 2015. Statistical comparison of insar tropospheric correction techniques. Remote sensing of environment, 170, pp.40-47. https://doi.org/10.1016/j.rse.2015.08.035

Bell, J.W., Amelung, F., Ferretti, A., Bianchi, M. and Novali, F., 2008. Permanent scatterer insar reveals seasonal and long-term aquifer-system response to groundwater pumping and artificial recharge. water resources research, 44(2). https://doi.org/10.1029/2007wr006152

Biggs, J., Wright, T., Lu, Z. and Parsons, B., 2007. Multi-interferogram method for measuring interseismic deformation: denali fault, alaska. geophysical journal international, 170(3), pp.1165-1179. https://doi.org/10.1111/j.1365-246x.2007.03415.x

Braun, A., 2021. Retrieval of digital elevation models from sentinel-1 radar data - open applications, techniques, and limitations. open geosciences, 13, pp.532–569. https://doi.org/10.1515/geo-2020-0246

Cignetti, M., Manconi, A., Manunta, M., Giordan, D., De Luca, C., Allasia, P., and Ardizzone, F., 2016. Taking advantage of the esa g-pod service to study ground deformation processes in high mountain areas: a valle d'aosta case study, northern Italy. Remote sensing, 8(10), pp.852. https://doi.org/10.3390/rs8100852

Delgado Blasco, J.M., Foumelis, M., Stewart, C. and Hooper, A., 2019. Measuring urban subsidence in the Rome metropolitan area (Italy) with sentinel-1 snap-stamps persistent scatterer interferometry. remote sensing, 11(2), pp.129. https://doi.org/10.3390/rs11020129

Doin, M.P., Guillaso, S., Jolivet, R., Lasserre, C., Lodge, F., Ducret, G. and Grandin, R., 2011. Presentation of the small baseline nsbas processing chain on a case example: the etna deformation monitoring from 2003 to 2010 using envisat data. Proceedings of the fringe symposium, https://doi.org/10.1109/igarss.2011.6049316

Efron, B. and Tibshirani, R., 1986. Bootstrap methods for standard errors, confidence intervals, and other measures of statistical accuracy. statistical science, pp.54-75. https://doi.org/10.1214/ss%2f1177013815

Fan, H., Wang, L., Wen, B. and Du, S., 2021. A new model for three-dimensional deformation extraction with single-track insar based on mining subsidence characteristics. International journal of applied earth observation and geoinformation, 94, pp.1-12. https://doi.org/10.1016/j.jag.2020.102223

Farr, T.G., Rosen, P.A., Caro, E., Crippen, R., Duren, R., Hensley, S., Kobrick, M., Paller, M., Rodriguez, E. and Roth, L., 2007. The shuttle radar topography mission. reviews of geophysics, 45(2). https://doi.org/10.1029/2005rg000183

Gan, J., Hu, J., Li, Z., Yang, C., Liu, J., Sun, Q. and Zheng, W., 2018. Mapping three-dimensional co-seismic surface deformations associated with the 2015 mw7.2 murghab earthquake based on insar and characteristics of crustal strain. science China earth sciences, 61(10), pp.1451-1466. https://doi.org/10.1007/s11430-017-9235-4

Hamlyn, J., Wright, T., Walters, R., Pagli, C., Sansosti, E., Casu, F., Pepe, S., Edmonds, M., Mccormick Kilbride, B., Keir, D., Neuberg, J. and Oppenheimer, C., 2018. What causes subsidence following the 2011 eruption at nabro (eritrea), progress in earth and planetary science, 5(1), pp.31. https://doi.org/10.1186/s40645-018-0186-5

Hoffmann, J., Zebker, H.A., Galloway, D.L. and Amelung, F., 2001. Seasonal subsidence and rebound in las vegas valley, nevada, observed by synthetic aperture radar interferometry. water resources research, 37(6), pp.1551-1566. https://doi.org/10.1029/2000wr900404

Hooper, A., Bekaert, D., Spaans, K. and Arıkan, M., 2012. Recent advances in sar interferometry time series analysis for measuring crustal deformation. Tectonophysics, 514-517, pp.1-13. https://doi.org/10.1016/j.tecto.2011.10.013

Jackson, J. and Fitch, T., 1981. Basement faulting and the focal depths of the larger earthquakes in the Zagros mountains (Iran). Geophysical journal international, 64(3), pp.561-586. https://doi.org/10.1111/j.1365-246x.1981.tb02685.x

Kirui, P.K.E., Reinosch, E., Isya, N., Riedel, B. and Gerke, M., 2021. Mitigation of atmospheric artefacts in multi temporal insar: a review. Journal of photogrammetry, remote sensing and geoinformation science, 89(3), pp.251-272. https://doi.org/10.1007/s41064-021-00138-z

Lohman, R.B. and Simons, M., 2005. Some thoughts on the use of insar data to constrain models of surface deformation: noise structure and data downsampling. geochemistry, geophysics, geosystems, 6(1). https://doi.org/10.1029/2004gc000841

López-Quiroz, P., Doin, M.P., Tupin, F., Briole, P. and Nicolas, J.M., 2009. Time series analysis of mexico city subsidence constrained by radar interferometry. Journal of applied geophysics, 69(1), pp.1-15. https://doi.org/10.1016/j.jappgeo.2009.02.006

Luo, H. and Chen, T., 2016. Three-dimensional surface displacement field associated with the 25 April 2015 gorkha, nepal, earthquake: solution from integrated insar and gps measurements with an extended sistem approach. remote sensing, 8(7), pp.1-14. https://doi.org/10.3390/rs8070559

Morishita, Y., 2021. Nationwide urban ground deformation monitoring in japan using sentinel-1 licsar products and licsbas. Progress in earth and planetary science, 8(1), pp.1-23. https://doi.org/10.1186/s40645-020-00402-7

Morishita, Y., Lazecky, M., Wright, T.J., Weiss, J.R., Elliott, J.R. and Hooper, A., 2020. Licsbas: an open-source insar time series analysis package integrated with the licsar automated sentinel-1 insar processor. remote sensing, 12(3), pp.1-24. https://doi.org/10.3390/rs12030424

Motagh, M., Beavan, J., Fielding, E.J. and Haghshenas, M., 2014. Postseismic ground deformation following the september 2010 darfield, new zealand, earthquake from terrasar-x, cosmo-skymed, and alos insar. Ieee geoscience and remote sensing letters, 11(1), pp.186-190. https://doi.org/10.1109/lgrs.2013.2251858

Nissen, E., Ghods, A., Karasözen, E., Elliott, J.R., Barnhart, W.D., Bergman, E.A., Hayes, G.P., Jamal-Reyhani, M., Nemati, M., Tan, F., Abdulnaby, W., Benz, H.M., Shahvar, M.P., Talebian, M. and Chen, L., 2019. The 12 november 2017 mw 7.3 ezgeleh-sarpolzahab (Iran) earthquake and active tectonics of the lurestan arc. journal of geophysical research: solid earth, 124(2), pp.2124-2152. https://doi.org/10.1029/2018jb016221

Osmanoğlu, B., Sunar, F., Wdowinski, S. and Cabral-Cano, E., 2016. Time series analysis of insar data: methods and trends. Isprs journal of photogrammetry and remote sensing, 115, pp.90-102. https://doi.org/10.1016/j.isprsjprs.2015.10.003

Parker, A., Biggs, J., Walters, R., Ebmeier, S., Wright, T., Teanby, N. and Lu, Z., 2015. Systematic assessment of atmospheric uncertainties for insar data at volcanic arcs using large-scale atmospheric models: application to the cascade volcanoes, united states. remote sensing of environment, 170, pp.102-114. https://doi.org/10.1016/j.rse.2015.09.003

Pawluszek-Filipiak, K. and Borkowski, A., 2020. Integration of dinsar and sbas techniques to determine mining-related deformations using sentinel-1 data: the case study of rydułtowy mine in poland. Remote sensing, 12(2), pp.242. https://doi.org/10.3390/rs12020242

Potin, P., Rosich, B., Miranda, N., Grimont, P., Shurmer, I., O'Connell, A., Krassenburg, M. and Gratadour, J.B., 2018. Sentinel-1 constellation mission operations status. igarss 2018 ieee international geoscience and remote sensing symposium, pp.1547-1550. https://doi.org/10.1109/igarss.2018.8517743

Qu, F., Lu, Z., Kim, J.W. and Zheng, W., 2019. Identify and monitor growth faulting using insar over northern greater houston, Texas, USA. Remote sensing, 11(12), pp.1498. https://doi.org/10.3390/rs11121498

Sharland, P.R., Casey, D.M., Davies, R.B., Simmons, M.D. and Sutcliffe, O.E., 2004. Arabian plate sequence stratigraphy revisions geoarabia, 9(1), pp.199-214. https://doi.org/10.2113/geoarabia0901199

Shi, X., Zhang, L., Zhong, Y., Zhang, L. and Liao, M., 2020. Detection and characterization of active slope deformations with sentinel-1 insar analyses in the southwest area of shanxi, China. Remote sensing, 12(3), pp.392. https://doi.org/10.3390/rs12030392

Sousa, J.J., Ruiz, A.M., Hooper, A.J., Hanssen, R.F., Perski, Z., Bastos, L.C., Gil, A.J., Galind Zaldívar, J., Galdeano, C.S.D., Alfaro, P., Garrido, M.S., Armenteros, J.A., Giménez, E. and Avilés, M., 2014. Multi-temporal insar for deformation monitoring of the granada and padul faults and the surrounding area (betic cordillera, southern Spain). procedia technology, 16, pp.886-896. https://doi.org/10.1016/j.protcy.2014.10.040

Vajedian, S., Motagh, M., Mousavi, Z., Motaghi, K., Fielding, E., Akbari, B., Wetzel, H.U. and Darabi, A., 2018a. Coseismic deformation field of the mw 7.3 12 november 2017 sarpol-e zahab (Iran) earthquake: a decoupling horizon in the northern Zagros mountains inferred from insar observations. remote sensing, 10, PP.1589. https://doi.org/10.3390/rs10101589

Vajedian, S., Motagh, M., Mousavi, Z., Motaghi, K., Fielding, E.J., Akbari, B., Wetzel, H.U. and Darabi, A., 2018b. Coseismic deformation field of the mw 7.3 12 November 2017 sarpol-e zahab (Iran) earthquake: a decoupling horizon in the northern Zagros mountains inferred from insar observations. remote sensing, 10(10), PP.1589. https://doi.org/10.3390/rs10101589

Vergés, J., Saura, E., Casciello, E., Fernàndez, M., Villaseñor, A., Jiménez-Munt, I. and García-Castellanos, D., 2011. Crustal-scale cross-sections across the NW Zagros belt: implications for the Arabian margin reconstruction. Geological magazine, 148(5-6), pp.739-761. https://doi.org/10.1017/s0016756811000331

Vernant, P., Nilforoushan, F., Hatzfeld, D., Abbassi, M.R., Vigny, C., Masson, F., Nankali, H., Martinod, J., Ashtiani, A., Bayer, R., Tavakoli, F. and Chéry, J., 2004. Present-day crustal deformation and plate kinematics in the middle east constrained by gps measurements in Iran and northern Oman. geophysical journal international, 157(1), pp.381-398. https://doi.org/10.1111/j.1365-246x.2004.02222.x

Washaya, P. and Balz, T., 2018. Sar coherence change detection of urban areas affected by disasters using sentinel-1 imagery. isprs int. Arch. photogramm. remote. sens. spat. inf. sci, pp.1857-1861. https://doi.org/10.5194/isprs-archives-xlii-3-1857-2018

Wegmüller, U., Werner, C.L., Stroozzi, T., Wiesmann, A., Frey, O. and Santoro, M., 2015. Sentinel-1 support in the gamma software. http://dx.doi.org/10.5270/fringe2015.pp70

Weike, L. and Goulin, L., 2013. A new method of weight choice in insar least squares unwrapping. Geodesy and geodynamics, 4(1), pp.35-40. https://doi.org/10.3724/sp.j.1246.2013.01035

Werner, C.L., Wegmüller, U., Strozzi, T. and Wiesmann, A., 2000. Gamma sar and interferometric processing software. http://dx.doi.org/10.1109/igarss.1998.699687

Yu, C., Li, Z., Penna, N.T. and Crippa, P., 2018. Generic atmospheric correction model for interferometric synthetic aperture radar observations. Journal of geophysical research: solid earth, 123(10), pp.9202-9222. https://doi.org/10.1029/2017jb015305

Yu, C., Penna, N.T. and Li, Z., 2017. Generation of real-time mode high-resolution water vapor fields from gps observations. Journal of geophysical research: atmospheres, 122(3), pp.2008-2025. https://doi.org/10.1002/2016jd025753

Zan, F.D., Zonno, M. and López-Dekker, P., 2015. Phase inconsistencies and multiple scattering in sar interferometry. Ieee transactions on geoscience and remote sensing, 53(12), pp.1-10. https://doi.org/10.1109/tgrs.2015.2444431

Zebker, H.A., Rosen, P.A. and Hensley, S., 1997. Atmospheric effects in interferometric synthetic aperture radar surface deformation and topographic maps. journal of geophysical research: solid earth, 102(b4), pp.7547-7563. https://doi.org/10.1029/96jb03804

Zhou, Z., Li, Z., Waldron, S. and Tanaka, A., 2019. InSAR time series analysis of l-band data for understanding tropical peatland degradation and restoration. Remote sensing, 11(21), pp.1-15. https://doi.org/10.3390/rs11212592